UNIVERSITY OF TWENTE

BACHELOR THESIS

Design of an Electric Circuit using Thin Film Transistors and Fuel Cells to Generate a Magnetic Moment

Justin Harbers
Faculty of Science and Technology

Committee Chair: DR. A. SUSARREY ARCE
Daily Supervisor: DR. I.S.M. KHALIL
External Member: DR. J. Dasdemir PhD

February 27, 2024

Abstract

The purpose of this thesis was to design an electric circuit that would generate a fluctuating magnetic moment in two coils that would allow an autonomous tetherless miniature robot to rotate in a static external magnetic field. This electric circuit was designed using Thin Film Transistors (TFTs) and Fuel Cells (FCs) to allow for a compact design while also retaining the autonomous aspect of the robot. The TFTs were characterised through experiments and compared to their discrete counterparts. These results depicted that they could be an essential component in the development of a miniature robot, due to their smaller size and lower energy consumption. The FCs allow the miniature robot to have an on-board power supply, which increases its autonomy, mobility and functionality. The goal of the compact design of the tetherless miniature robot is to allow it to be used for, for example, drug delivery in the body. The components were incorporated into an electric circuit, which was tested and compared to the simulation. Some changes had to be made to allow the circuit to function properly when compared to the original design. Afterwards, suggestions for improvements and further research questions were stated based on the results of the comparison.

List of Figures

List of Tables

CONTENTS

I. Introduction

The human body is susceptible to several diseases or afflictions that require surgical intervention. These procedures can contain inherent risks for vulnerable patients, such as the elderly [1]. To reduce these risks as much as possible, minimally invasive procedures are used, which can have the benefits of "reduction of recovery time, medical complications, infection risks and postoperative pain" as explained by Nelson et al [2]. Miniature robots allow for minimally invasive interventions in the human body. Depending on the size, they could potentially be used for the removal of polyps during a colonoscopy [2], precise drug delivery [3] and minimally invasive surgeries [4].

Due to their small size, most microrobots do not have the space to allow for an on-board power supply or control [5]. Rather, most of the control and actuation of the microrobot is done through off-board processes [5]. These microrobots can navigate the body using, for example, external magnetic fields with the help of interventional devices such as catheters, guidewires and endoscopes [6]. Due to the presence of these tethers, however, the microrobots are limited in their degrees of freedom (DOF) [2]. Furthermore, tethered microrobots are limited in the areas they can reach in the human body [2]. The lack of an on-board power supply reduces the necessary size, but also takes away the autonomy of the microrobot, which limits the range of functions it can perform [5].

Currently, there is a lot of research being done in the field of the development of microrobots. For example, Seyfried et al. [7] have tried to develop a swarm of 1000 2x2x1 mm^3 microrobots, with an on-board power supply, an insect-like walking mechanism and the ability to perform small tasks. However, this proved to be very challenging and in the end, was not successful. It did, however, provide them with a starting point to improve upon [7]. Estaña et al. [8] have successfully developed untethered and independent microrobots with a size of less than 1 cm^3, which can also perform small tasks. These are powered using a power floor by using magnetic fields and communicate using infrared [8]. However, due to the nature of the energy supply, these can not be used in the human body.

An essential component of the microrobot is therefore the power supply. A normal battery could be used, but due to fuel depletion, the voltage output of a battery is neither constant nor endless [9]. The use of a fuel cell (FC) would eliminate these disadvantages. An FC is a device that uses electrochemical reactions to generate electricity [10] and has a constant output [9]. Implantable medical devices (IMDs), such as pacemakers, drug pumps and blood glucose meters require stable and efficient power [10]. These IMDs are traditionally supplied with lithium-ion batteries, which occasionally need to be replaced. This process is inefficient in terms of medical costs and can be painful for the patient. An alternative could be the use of FCs, which are efficient in the conversion of energy, have mild operating conditions, great biocompatibility and do not need to be replaced from time to time, since they could use substances found within the body as fuel [10].

Soft robots could also be used instead of microrobots. Recent advancements in soft materials have allowed soft robots for new possible applications in the biomedical field [11]. Different levels of biocompatibility and biomimicry allow for several medical applications, such as soft tools for surgery, prostheses, artificial organs and drug delivery [11]. Soft materials can be used for remote target areas of drug delivery, where normal endoscopic or surgical tools prove ineffective. This could be the case for the inner parts of the brain, liver or pancreas [11].

This thesis will attempt to develop an electronic circuit that combines the concept of microrobots, with FCs and soft robotics (thin film transistors) to generate a magnetic moment. This could, for example, be used to allow a microrobot to rotate in a magnetic field. First, the properties of these components will be analysed. After this, these components will be incorporated into the design of an electric circuit. Finally, this circuit will be tested and compared to the simulations.

II. Methodology

A. Fuel Cell

Fuel Cells use electrochemical reactions to generate electricity. In this case, the electrochemical reaction between hydrogen and oxygen generates electricity, where water is formed as a product of these half-reactions [12]. These reactions are as follows:

$$2\,H_2 \longrightarrow 4\,H^+ + 4\,e^- \tag{1}$$

$$O_2 + 4\,e^- + 4\,H^+ \longrightarrow 2\,H_2O \tag{2}$$

An FC is composed of an anode, a cathode and an electrolyte [10]. The reaction starts in the anode, where protons and electrons are released. These protons are transported through the electrolyte to the cathode [10]. By spatially separating the anode and the cathode, the protons that were generated can flow through an external circuit [9, 10]. When incorporated into a microrobot, the FCs have a certain advantage when compared to batteries.

FCs are considered "open" thermodynamic systems and operate at a thermodynamic steady state [9]. This means that the output of the FCs will remain constant as long as it is continually supplied with fuel. Batteries, however, are a "closed" thermodynamic system. This means that batteries have a decrease in output over time as the fuel is depleted from the battery [9].

In a water container, H_2O can be continuously supplied to the FCs. To make use of the H_2O, the H_2 needs to be separated so that it can be used in reaction (1). This

is done through electrolysis using a Proton Exchange Membrane (PEM) electrolyzer (Horizon PEM Blue Electrolyzers, FCSU-010 model). Using an external power supply, the H_2 is generated in the following reactions:

$$2\,H_2O \longrightarrow 4\,H^+ + 4\,e^- + O_2 \quad (3)$$

$$4\,e^- + 4\,H^+ \longrightarrow 2\,H_2 \quad (4)$$

Together with end plates, gaskets, current collectors, Flow Field Plates (FFPs) and Membrane Electrode Assemblies (MEAs), the FC can be constructed.

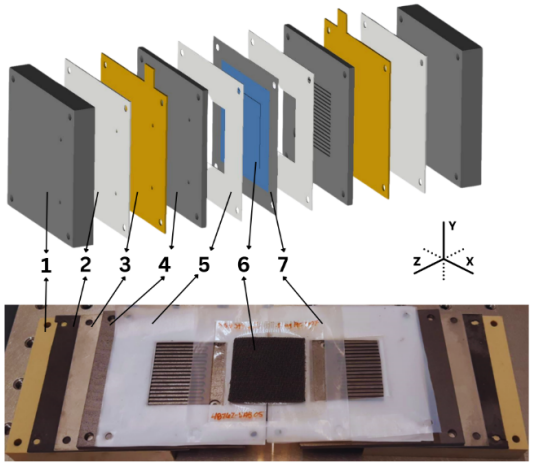

Figure 1: Schematic view of the Fuel Cell, with the components: End plate of the FC (1), sealing gasket (2), current collector (3), flow field plate (4) (active area 3.5x3.5 cm^2), gasket (5), membrane electrode assembly (6), teflon frame (7).

The structure of the FC is depicted in Figure 1. The end plates (1) cause uniform compression across the FC. They are made of polyetheretherketone (PEEK), which has a high permeation resistance against hydrogen [13]. The sealing gasket (2) and gasket (5) are there to prevent leakage and act as a seal. The current collectors (3) are made out of stainless steel (SS316L). The FFPs (4) are made out of graphite, which has a high conductivity, and distribute the reactants evenly across the electrodes. The MEA (6) consists of a Gas Diffusion Layer (GDL), a catalyst and the PEM. The GDL consists of a carbon cloth which helps the permeation of gaseous reactants. The FC was assembled using stainless steel bolts and M3 nuts, both wrapped in PTFE Thread Seal Tape Teflone (T-27730A) to prevent the current collectors from short-circuiting.

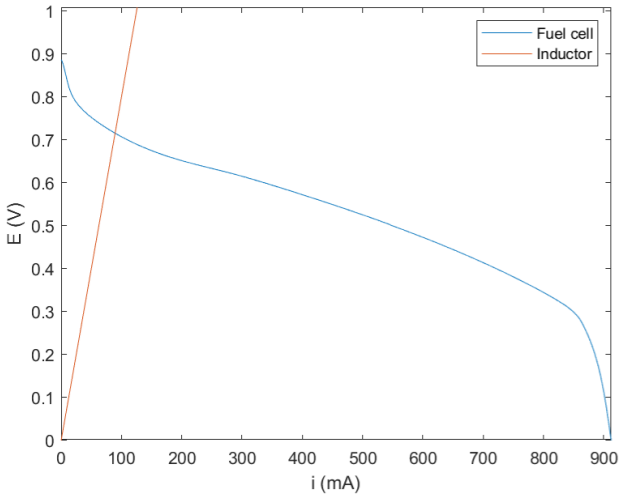

Figure 2: IV characteristics of the Fuel Cell with an active area of 3.5x3.5 cm^2 together with a ferrite power inductor [14]

Figure 2 depicts the IV characteristics of the FC together with a ferrite power inductor [14]. The voltage of the FC decreases with an increasing current. The coil has an internal resistance of 8 Ω, which explains the linear relationship (Ohm's law) between the current and the voltage. The intersection of the lines depicts the operating region of the FC. Both the FC and the ferrite power inductor will be implemented in the design, which is further discussed in section II-C (Electric Circuit). These components will be incorporated in a spherical capsule, of which the diameter is estimated to be 64 mm to provide an adequate fit for the FC.

B. Thin Film Transistor

Thin Film Transistors (TFTs) are a subset of Metal-Oxide-Semiconductors Field-Effect Transistors (MOSFETs), which typically consist of metallic contacts, a dielectric layer, a semiconducting layer and an insulating substrate [15]. A MOSFET is a voltage-controlled switch, where the conductivity between the source and the drain terminals is determined by the voltage applied to the gate terminal. The main purpose of the MOSFET is to act as a switch, but it can also be used as an amplifier and for signal inversion.

There are two types of MOSFETs, namely N-type and P-type. N-type MOSFETs consist of a P-type substrate with two heavily doped N-type regions for the gate and the source. This will result in the formation of PN-junctions between the substrate and these regions. A depletion region will naturally form at PN-junctions when there is no gate-source voltage (V_{gs}) and the MOSFET is operating in the cutoff region. An insulating layer with a metallic contact is added onto the substrate, which acts as a gate region. When there is a positive V_{gs}, holes in the substrate will be repelled from the gate. As a result, electrons will be attracted to the positive V_{gs}. This creates a channel between the source and the drain. With a larger V_{gs}, an inversion layer of electrons starts to form at the source terminal which expands towards the drain terminal. When the V_{gs} is larger than the voltage threshold (V_{th}), the inversion layer will have reached the drain terminal and current will start to flow between the source and the drain terminal when a voltage is applied between the source and the drain (V_{ds}). The channel width is determined by the value of V_{gs}, with a larger V_{gs}, the channel will be wider as well, which allows for more current to flow between the source and the drain. A P-type MOSFET works on the same principle, but it has an N-type substrate with two heavily doped P-type regions. When a V_{gs} is applied, electrons will be repelled from the gate terminal and holes will act as the current carriers.

Aside from the type, a MOSFET can also have two different modes. These are the enhancement mode and the depletion mode. The previous example is that of an enhancement mode MOSFET, which is normally off at a V_{gs} of zero. A depletion mode MOSFET is normally on for a V_{gs} of zero. This means that a negative V_{gs} would have to be applied to actively turn the MOSFET off.

The TFTs that will be used in this thesis are of the N-type. They were not commercially produced, and therefore were not provided with a datasheet. The metallic contacts of the TFT consist of 60 nm Au on top of 10 nm Ti. The rest of the structures on the TFT are passivated with a layer of 25 nm Al_2O_3. The TFT itself and the layout are visible in Figures 3a and 3b.

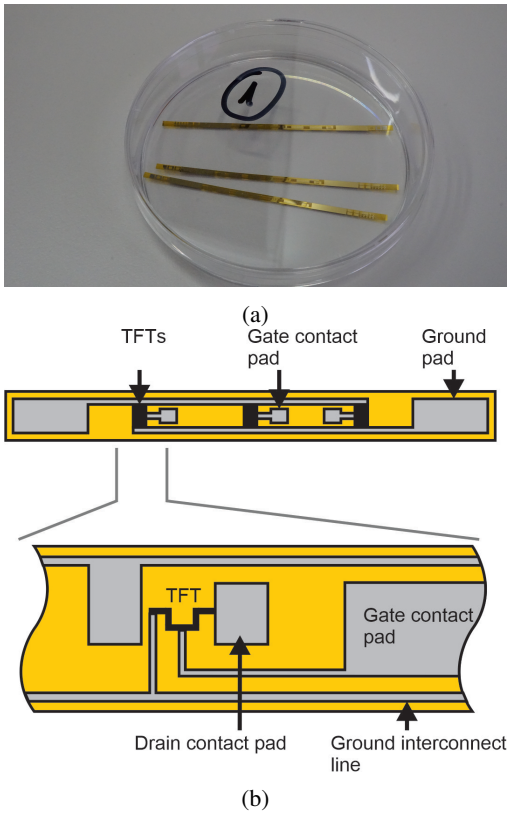

Figure 3: (a) Image of the Thin Film Transistors (TFTs). The TFT has a length of around 6 cm and a width of around 2 mm. (b) Layout of the TFTs. The whole TFT consists of 3 Drain and Gate contact pads, with a common Ground pad that is interconnected with the rest.

Since there is no datasheet of the TFT, some parameters have to be determined through experiments to allow for integration into an electric circuit. Aside from that, the TFT will also have to be compared to a normal MOSFET (VN2222L) to compare how both parts behave at the desired voltages. A probe station along with a Keithley 4200a-scs parameter analyser was used to conduct these tests. The probe station allows for precise needle placement to replicate an electric circuit to allow for precise measurements of a single part. The Keithley parameter analyser can be used to precisely show the reaction of the part to a change in a parameter.

Firstly, The current-voltage characteristics (IV curves) of the MOSFET analysed through the experiment will be compared to the IV curves provided in the datasheet of the same MOSFET. This is done to determine the accuracy of the parameter analyser. To measure the IV curves, the drain current (I_{ds}) is measured while setting the V_{gs} to a certain value (between 1.2 V and 2 V) and performing a linear voltage sweep (from 0 V to 2 V) on the V_{ds}. These results are given in Figures 4a and 4b.

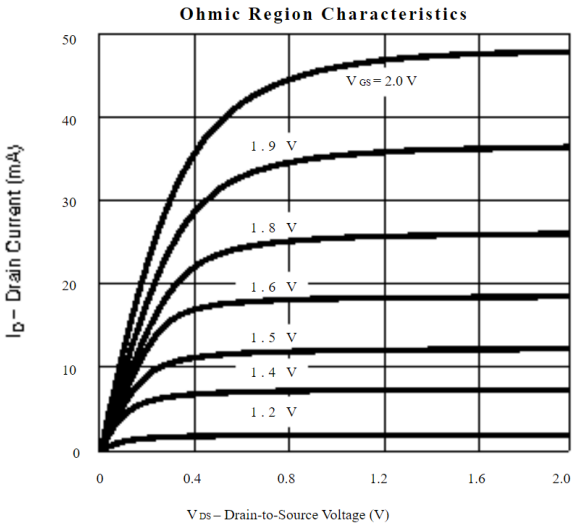

(a)

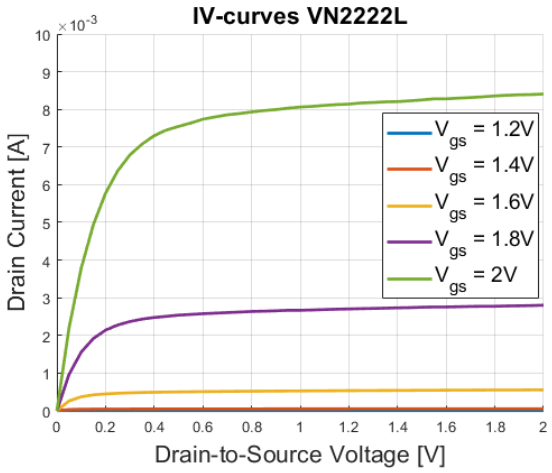

(b)

Figure 4: (a) IV curves of the VN2222L MOSFET provided in the datasheet [16]. (b) The drain current (I_{ds}) was measured for several gate voltages (V_{gs}), while performing a linear voltage sweep on the drain-to-source voltage (V_{ds}) from 0 V to 2 V.

These figures show that the experimental measurements of the MOSFET (Figure 4b) do not correspond to those of the datasheet (Figure 4a). A reason for this might be that the parameter analyser might prove to be slightly inaccurate when working with low voltages.

Second, the V_{th} for both the MOSFET and the TFT were determined. This is done by setting the V_{ds} to zero and performing a linear voltage sweep for the V_{gs} to measure at what value I_{ds} starts to flow. These results are depicted in Figures 5a and 5b.

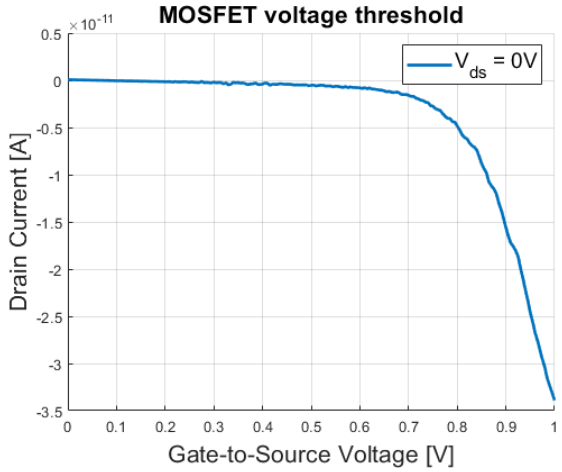

(a)

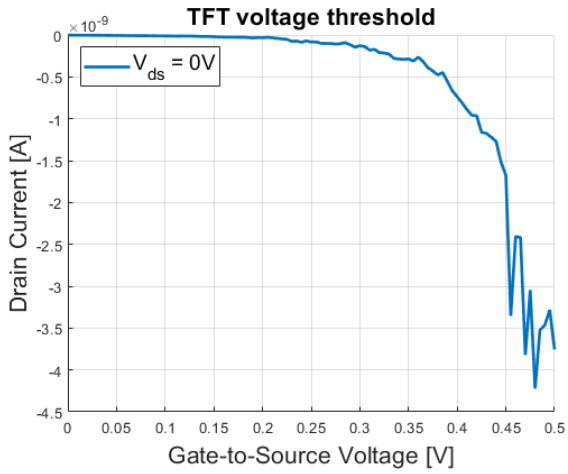

(b)

Figure 5: (a) Voltage threshold measurement of the MOSFET. This is done by setting the drain-to-source voltage to zero, while performing a linear voltage sweep on the gate-to-source voltage from 0 V to 1 V and measuring the drain current. (b) Voltage threshold measurement of the TFT. This is done by setting the drain-to-source voltage to zero, while performing a linear voltage sweep on the gate-to-source voltage from 0 V to 0.5 V and measuring the drain current.

As depicted in Figure 5a, the V_{th} of the MOSFET is around 0.5 V, which roughly corresponds to that of the datasheet (0.6 V to 2.5 V [16]). The V_{th} for the TFT seems to be between 0.2 V and 0.25 V as is visible in Figure 5b.

Thirdly, the I_d leakage for both the MOSFET and the TFT was determined. This is done by setting the V_{gs} to zero, applying a V_{ds} and measuring the resulting I_d. These results are depicted in Figures 6a and 6b.

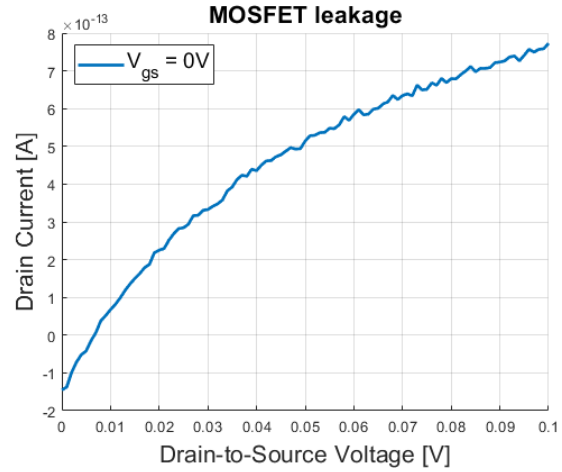

(a)

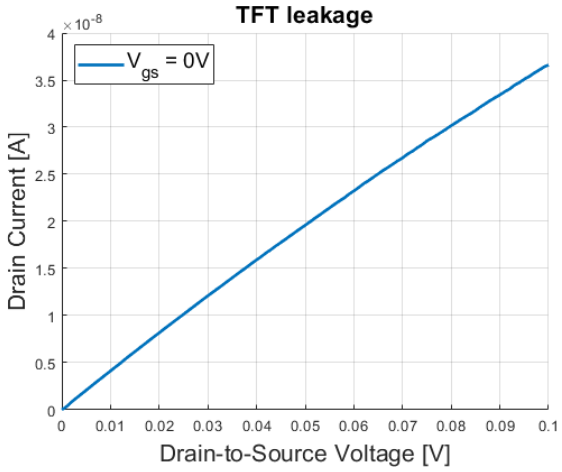

(b)

Figure 6: (a) I_d leakage measurement of the MOSFET. This is done by setting the gate-to-source voltage to zero, while performing a linear voltage sweep on the drain-to-source voltage from 0 V to 0.1 V and measuring the drain current. (b) I_d leakage measurement of the TFT. This is done by setting the gate-to-source voltage to zero, while performing a linear voltage sweep on the drain-to-source voltage from 0 V to 0.1 V and measuring the drain current.

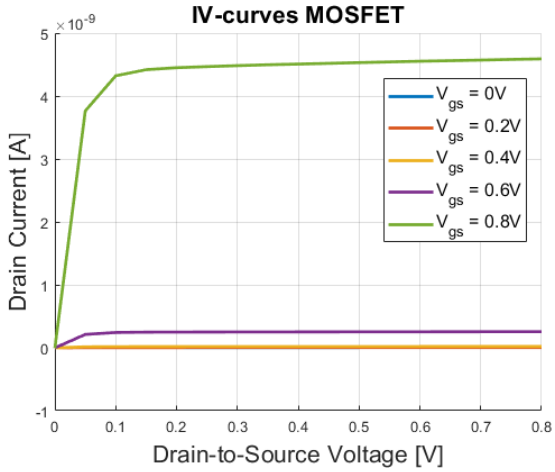

(a)

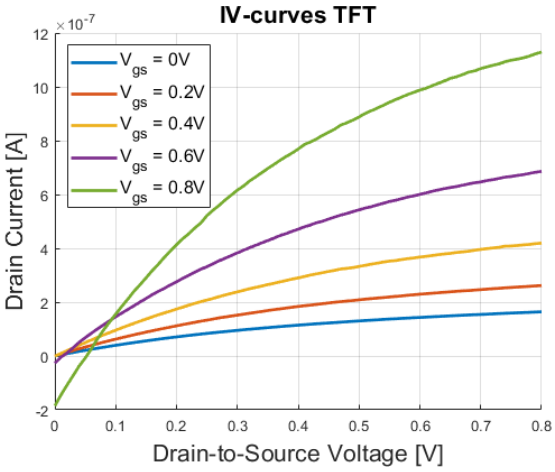

(b)

Figure 7: (a) The drain current (I_{ds}) for the MOSFET was measured for several gate voltages (V_{gs}), while performing a linear voltage sweep on the drain-to-source voltage (V_{ds}) from 0 V to 0.8 V. (b) The drain current (I_{ds}) for the TFT was measured for several gate voltages (V_{gs}), while performing a linear voltage sweep on the drain-to-source voltage (V_{ds}) from 0 V to 0.8 V.

As depicted in Figure 6a, the amount of leakage for the MOSFET is of negligible size. While on the other hand the leakage for the TFT, as shown in Figure 6b is considerably larger than that of a normal MOSFET.

Lastly, the IV curves of the MOSFET and the TFT for low voltages were measured. These voltages range from 0 V to 0.8 V, since this corresponds to the operating region of the FCs. The principle behind these measurements is the same as for the measurements given in Figure 4b. The results of these measurements are depicted in Figures 7a and 7b.

Figures 7a and 7b depict the resulting I_d as a result of a certain V_{gs} and V_{ds}. Looking at the drain current of both the MOSFET and the TFT, it is clear that the resulting drain current for low voltages is higher for the TFT (as visible in Figure 7b) than for the MOSFET (as visible in Figure 7a). From this, the conclusion can be made that the TFT would provide better results at the operating voltages of a singular FC.

The FCs can also be stacked up to 3 times to provide a larger voltage (1,6 V and 2,4 V), this might be useful in circuits where there is a requirement for a larger voltage source than what a single FC can provide (0,8 V). The IV curves corresponding to larger voltages are depicted in Figures 8a and 8b.

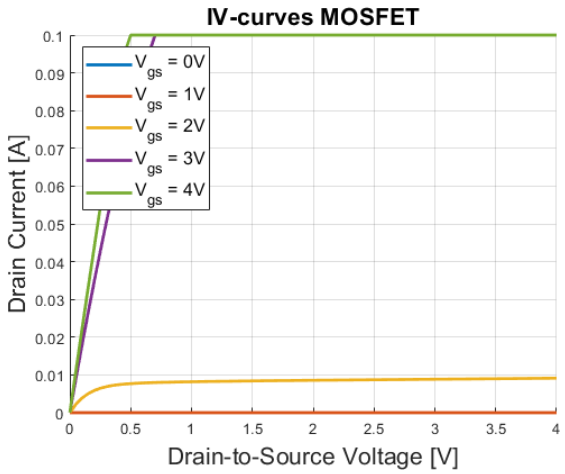

(a)

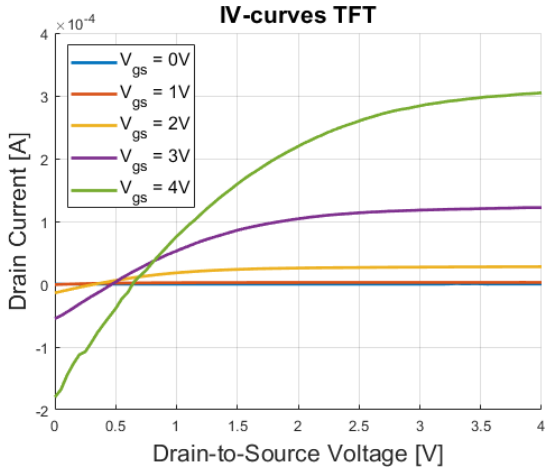

(b)

Figure 8: (a) The drain current (I_{ds}) for the MOSFET was measured for several gate voltages (V_{gs}), while performing a linear voltage sweep on the drain-to-source voltage (V_{ds}) from 0 V to 4 V. (b) The drain current (I_{ds}) for the TFT was measured for several gate voltages (V_{gs}), while performing a linear voltage sweep on the drain-to-source voltage (V_{ds}) from 0 V to 4 V.

Figures 8a and 8b show that a normal MOSFET would work better for larger voltages above a certain point, since it allows for a larger drain current.

C. Electric Circuit

The electric circuit should incorporate the concept of a microrobot, the FCs and the TFT to create a design that generates a magnetic moment. This magnetic moment could be incorporated into a capsule to allow for rotation when accompanied by external magnetic fields. To generate a magnetic moment inside the capsule a ferrite power inductor will be used [14]. This is a small coil that can be incorporated into a microrobot and used to generate a magnetic field when current is flowing through it. This magnetic field can interact with external magnetic fields and change their orientation accordingly. A schematic view of this design is given in Figure 9.

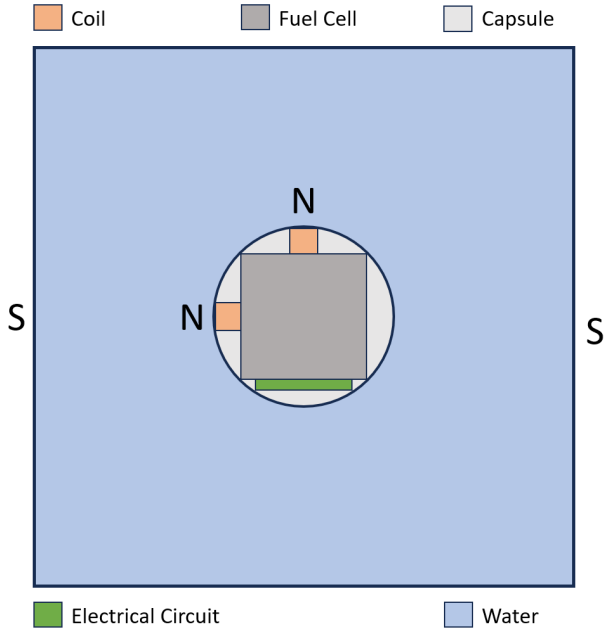

Figure 9: Schematic top view of the design. The capsule is placed in a water tank with magnetic south poles on either side of the tank. The coils in the capsule will generate a magnetic north pole. The FC will generate a voltage which will flow through the electric circuit and then to the coils accordingly.

To allow the design given in Figure 9 to rotate, the coils must be activated through an oscillatory signal and out of phase from one another. The external magnetic fields will be powered through an alternating current as well, which will be synchronised with the oscillations of the coils. By having only a singular external magnetic field at a time, it prevents the magnetic fields from cancelling out against each other [17]. When a coil is activated, it will be attracted by the magnetic field and rotate. At a certain point, it will not rotate any further, and then the other coil should be activated so that it is attracted by the magnetic field and rotates the capsule. This means that the electric circuit has several design requirements. These are given in Table I:

Requirement	Reason
Integrate the FCs and the TFT into the electric circuit.	Adding an on-board power supply and low power (soft) electronics is beneficial for the microrobot.
The electric circuit must fit inside of the capsule with the other components.	The size should be small enough to fit inside of the capsule with the FCs and the coils.
The FCs must be able to power the electric circuit.	The on-board power supply should provide sufficient power to the circuit.
The circuit must provide the coils with 100 mA.	The maximum according to the datasheet is 130 mA, 100 mA is chosen as a safe operating value. This creates a magnetic field.
Electric circuit must generate an oscillating, out-of-phase signal.	The coils both need an oscillating signal which does not interfere with the other to allow for rotation in an external magnetic field.
The frequency of the oscillating signal should be 0.1 Hz.	To allow for a smooth rotation of the capsule.
The duty cycle of the oscillating signal should be 50%.	To allow for an even rotation between both of the signals.

Table I: Overview of the requirements for the electric circuit.

These requirements can be incorporated into the design together with the FCs and the TFT. A schematic view of the electric flow chart is visible in Figure 10.

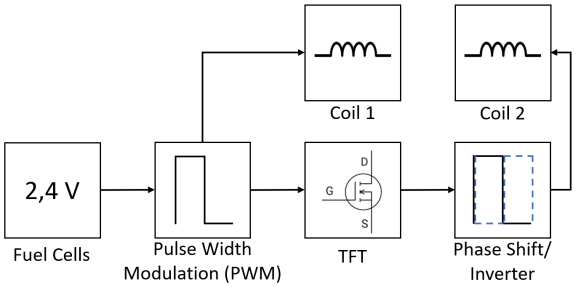

Figure 10: Schematic view of the electric flow chart. The voltage stemming from the FC is sent to a Pulse Width Modulation (PWM) unit. The PWM unit allows for the signal to oscillate at a frequency of 0.1 Hz and sends the signal to one of the coils and the TFT. From the TFT the signal then goes to the inverter, which gives a phase shift to one of the oscillatory signals. This is then sent to the other coil.

Using LTspice, the electric flow diagram depicted in Figure 10 can be converted to an electric circuit. This circuit is given in Figure 11.

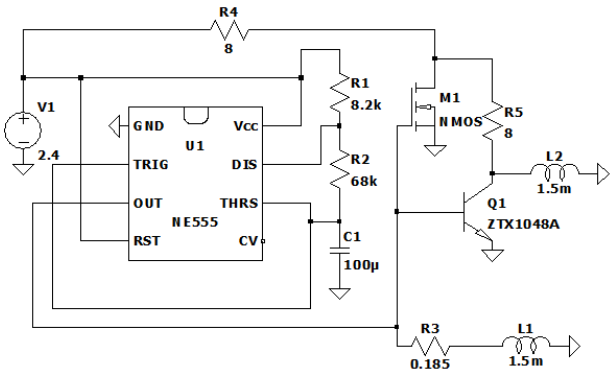

Figure 11: The electric circuit based on the schematic view given in Figure 10. The FCs are represented as a 2.4 V source. The FCs send a voltage to the oscillator (U1), which is set up to allow for 0.1 Hz (+0.048%) oscillation [18]. The output is sent to one of the coils (L1) and to the TFT (M1) and a transistor (Q1). The FC sends a DC voltage to the TFT, which goes to the transistor. The transistor inverts the oscillating output from U1 and sends it to the coil (L2)

Based on the requirements given in Table I, the frequency of the oscillations should be 0.1 Hz and the duty cycle should be around 50%. The frequency and duty cycle is determined using the following formulas [19]:

$$\text{Frequency [Hz]: } f = \frac{1}{T} = \frac{1.44}{(R_A + 2R_B)C} \tag{5}$$

$$\text{Duty cycle [\%]: } D = \frac{R_B}{R_A + 2R_B} \cdot 100\% \tag{6}$$

Where R_A corresponds to R_1, R_B corresponds to R_2 and C corresponds to C_1 in Figure 11. These values were chosen based on the values given in the datasheet [18]. Putting the values in equations (5) and (6) yields the following results:

$$f = \frac{1.44}{(8200 + 2 \cdot 68000) \cdot (100 \cdot 10^{-}6)} \approx 0.1 \text{ [Hz]} \tag{7}$$

$$D = \frac{68000}{8200 + 2 \cdot 68000} \cdot 100\% \approx 47\% \tag{8}$$

The output of the oscillator (U1) is a square wave signal that oscillates between 0 and 2.4 V. However, due to the base-emitter turn-on voltage of the ZTX1048A being typically 860 mV [20], the voltage output from the LMC555 is lowered as well. The voltage output now oscillates between 0 and 818.5 mV as a result. For a current of 100 mA to flow through the coil, an extra resistor has to be added, the value of which can be determined using Ohm's law:

$$(R_3 + R_{L1})\ [\Omega] = \frac{[\text{Voltage mV}]}{[\text{Current mA}]} = \frac{818,5}{100}$$
$$R_3 = \frac{818,5}{100} - R_{L1} = 8,185 - 8 = 0.185\ [\Omega]$$

Coil 2 (L2) is powered through the upper part of the circuit. The MOSFET (TFT) is set up to act as a switch and the transistor (Q1) acts as an inverter for the signal to introduce a phase shift, using the output from the timer. The resistances R_4, R_5 and R_{L2} are set up in series, thus their values can be determined in the same way as R_3.

$$(R_4 + R_5 + R_{L2})\ [\Omega] = \frac{[\text{Voltage mV}]}{[\text{Current mA}]} = \frac{2400}{100}$$
$$R_3 + R_4 = \frac{2400}{100} - R_{L1} = 24 - 8 = 16\ [\Omega]$$

This electric circuit can be simulated within LTspice to gain insight into the current flowing through both of the coils. The simulation is given in Figure 12.

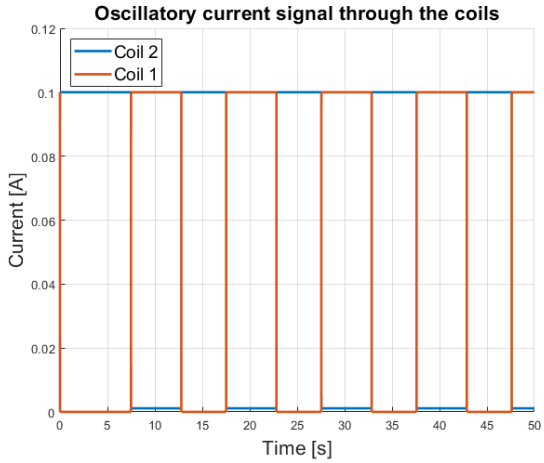

Figure 12: The oscillatory signal in both coils using the circuit given in Figure 11. Coil 1 (L1) oscillates between 0 and 100 mA. Coil 2 (L2) oscillates between 1 and 100 mA. Both coils operate at a frequency of 0.1 Hz. The timer has a 'start-up' period of 7.49 seconds.

The signal through both of the coils meets some of the requirements given in Table I since it oscillates out of phase and passes 100 mA through the coils. This circuit can be built on a breadboard for testing purposes. The size of the breadboard would be too large to fit into the capsule, so the circuit is designed onto a Printed Circuit Board (PCB). This is a small board used to wire different electric components to each other. The result of designing the electric circuit given in Figure 11 is given in Figure 13.

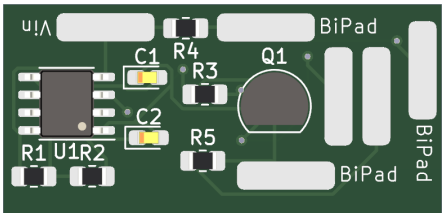

(a) PCB top-view.

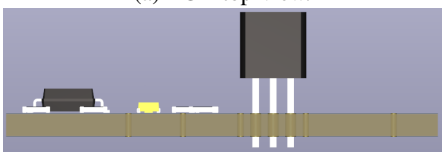

(b) PCB front-view.

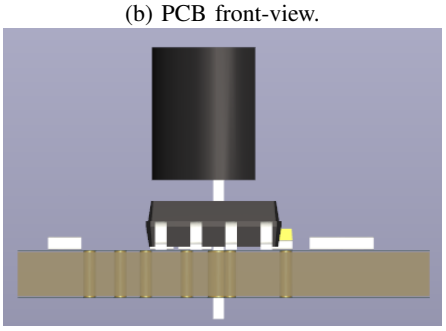

(c) PCB side-view.

Figure 13: Top (a), front (b) and side (c) view of the electric circuit depicted in Figure 11 integrated into a Printed Circuit Board (PCB)(31.36x14.88 mm^2). The output of the FCs are connected to the 'Vin' pad and the 'bi-directional' pads (BiPads) can be used to connect to the coils and the TFT.

Figure 13 depicts the result of converting the electric circuit given in Figure 11 to a PCB. This PCB contains the several components that can be found in the circuit together with a few pads, which can be used for soldering purposes. The voltage gained from the FCs can be connected to the V_{in}. The TFT can be connected to some of the 'BiPads', since the structure (which is shown in Figure 3a) does not allow it to be directly integrated into the PCB like the other components. Since the coils will also need to be placed at specific points in the capsule, they too cannot be directly integrated into the PCB, and therefore can be connected to the 'BiPads'.

This PCB meets the final remaining requirements given in Table I, since it allows the FCs and the TFT to be integrated into the circuit, its size of 31.36x14.88 mm^2 allows it to be incorporated into the capsule and it can be powered by an FC-stack.

III. Results

To test whether or not the electric circuit given in Figure 11 meets the requirements, the circuit was set up on a solderless breadboard.

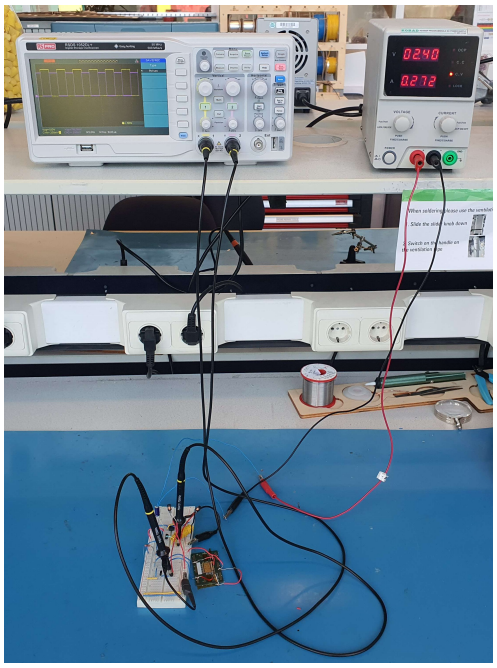

Figure 14: The breadboard based on the electric circuit given in Figure 11. With a DC power supply (KORAD KD3005P) and an oscilloscope (RS PRO RSDS 1052DL+).

The breadboard is set up together with a DC power supply (KORAD KD3005P [21]) and an oscilloscope (RS PRO RSDS 1052DL+ [22]). Since there is currently only a singular FC and not an FC-stack consisting of 3 FCs, the power supply is done through the use of the KORAD. The voltage of a singular FC would be 0.8 V, which would not be sufficient to power the circuit. The oscilloscope is used to measure the voltage over both of the coils and to collect the data.

The voltage from the power supply is connected to the power bus on the breadboard, while the ground is connected to the ground bus. Due to unforeseen circumstances, some changes were made on the breadboard when compared to the electric circuit given in Figure 11. Since the output current of the LMC555 timer ([19]) was way less than the idealised version of a 555 timer in LTspice, current amplifiers in the form of transistors (C547B [23] and BC549C [24]) were implemented into the circuit. These transistors were sourced from the same container, which led to the assumption that they were equivalent. However, subsequent analysis of the transistors after the measurements has shown that this was not the case. The BC549C transistor, which has a higher current gain, was used in the branch leading to coil 1, while the C547B transistor was used in the branch leading to coil 2. R_3 (in Figure 11) is replaced by a 100 mΩ resistor and a wound-up 132 cm wire (64.1 Ω/km [25]) in series to form roughly 185 mΩ resistance, due to the absence of the required 185 mΩ resistor.

A schematic overview of the breadboard setup is depicted in Figure 15.

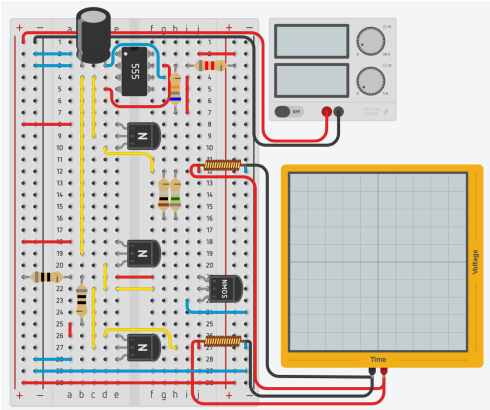

Figure 15: Schematic view of the breadboard, power supply and oscilloscope given in Figure 14.

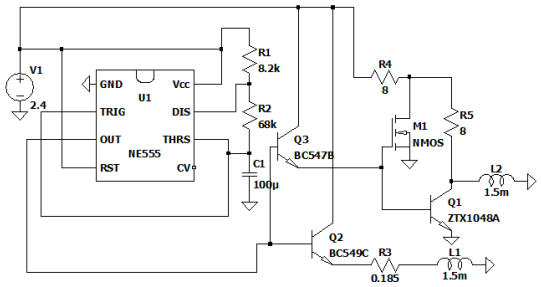

(a)

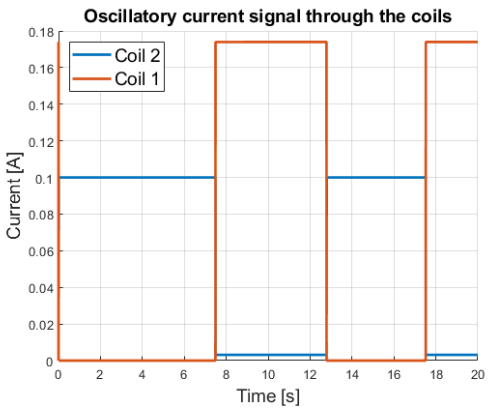

(b)

Figure 16: (a) The electric circuit based on the breadboard in Figure 15. (b) Simulation of the signal through the coils. Coil 1 oscillates between 0 and 173.98 mA, has a frequency of 0.0997 Hz and a duty cycle of 52.79%. Coil 2 oscillates between 3.11 and 99.99 mA, has a frequency of 0.0997 Hz and a duty cycle of 47.16%. The 'start-up' time is 7.49 seconds.

As a result of the changes made to the original design, the new electric circuit and its simulation are given in Figure 16a and Figure 16b respectively.

The oscilloscope was used to visualise the voltages over both of the coils, the result of which is depicted in Figure 17.

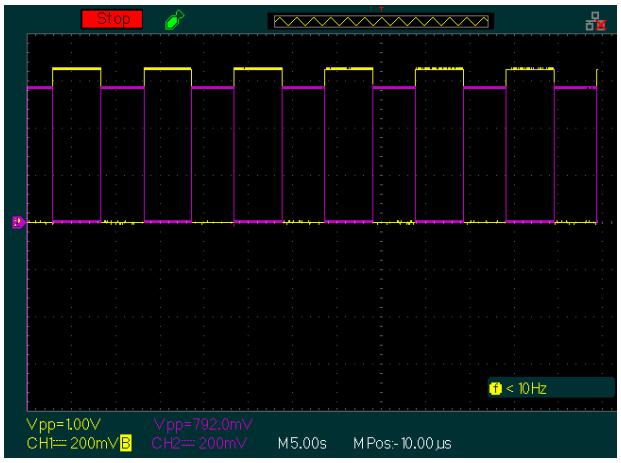

Figure 17: Voltages over coil 1 and coil 2, visualised using an oscilloscope (RS PRO RSDS 1052DL+), where the yellow waveform corresponds to coil 1 and the purple waveform corresponds to coil 2.

The voltage from Figure 17 was converted to amperage using Ohm's law, using the internal resistance of the coils (8 Ω [14]).

$$I = \frac{U}{R} = \frac{\text{Voltage}}{\text{Resistance Coil}} \tag{9}$$

The current through both of the coils can then be plotted, which is depicted in Figure 18a. The figure depicts a discrepancy between the measured currents through the coils. The oscillating current through coil 1 is greater than the current through coil 2. As explained earlier, this is likely because a transistor with a greater current gain was (unknowingly) used to boost the current through coil 1.

When comparing the results from the measurements (Figure 18a) with the simulation (Figure 18b), certain differences stand out. First, the current through the coils on the breadboard is smaller than the current flowing through the coils in the simulation. Second, the frequency of the signal of the breadboard is slightly off when compared to that of the simulation. It is visible that over time the signal slightly shifts with respect to its previous position. Third, the signal of the breadboard is noisier than the signal of the simulation. Lastly, the signal through the coils on the breadboard does not show a 'start-up' period when compared to the simulation. This might be because the measurement did not instantly start the moment the breadboard was supplied with power.

Some of these differences can be caused by imperfections present throughout the setup. The wires on the breadboard each have a small resistance, which might lower the overall signal strength of the circuit. The breadboard might also introduce noise to the signal [26].

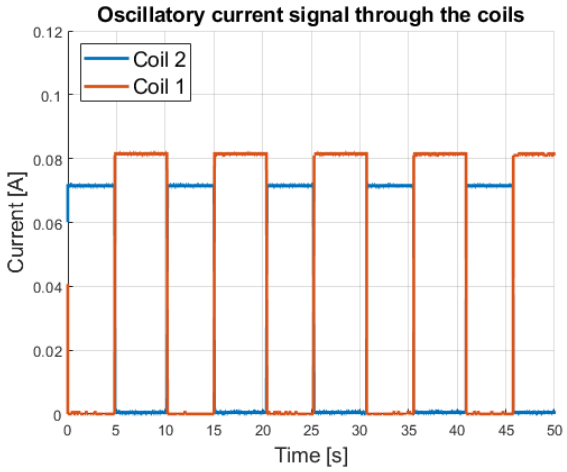

(a)

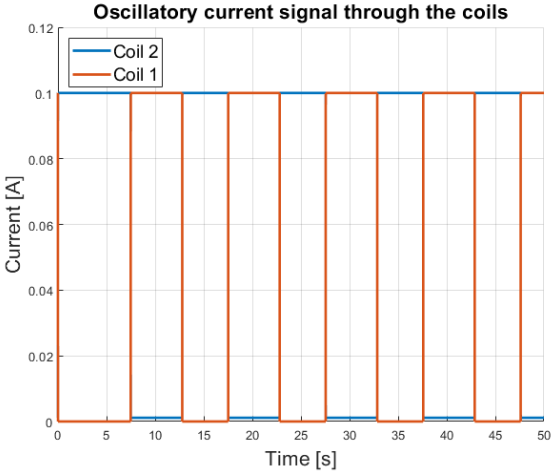

(b)

Figure 18: (a) Oscillatory current signal through both of the coils of the breadboard. The signal of coil 1 oscillates between 0-1 and 81-82 mA, while coil 2 oscillates between 0-1 and 71-72 mA. Both coils oscillate at a frequency of 0.0977 Hz. Coil 1 has a duty cycle of 52.77% and coil 2 has a duty cycle of 47.29%. (b) Figure 12.

A. *Parasitics*

From the comparison between Figure 18a and Figure 18b was determined that several aspects were different. This is due to the fact that the simulation in software like LTspice shows the ideal scenario, whereas a circuit built on a breadboard will show different characteristics. For example, wires that are used to connect different components on a breadboard all have their own resistances, which adds voltage losses to the circuit. A solderless breadboard can introduce noise into the signal [26] and

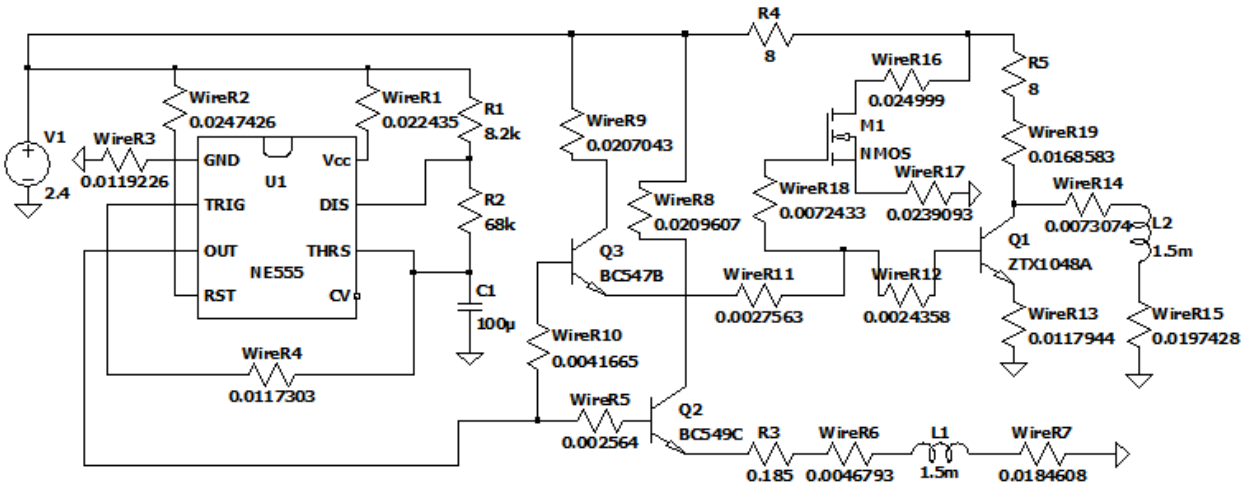

Figure 19: The electric circuit given in Figure 16a with the added wire resistances (possible resistances of the breadboard have been neglected).

some components, such as the LMC555, will not operate at their maximum capacity. To account for some of these parasitics, the resistances of each wire used on the breadboard were added to the simulation in LTspice. This is given in Figure 19 with the corresponding signal in Figure 20.

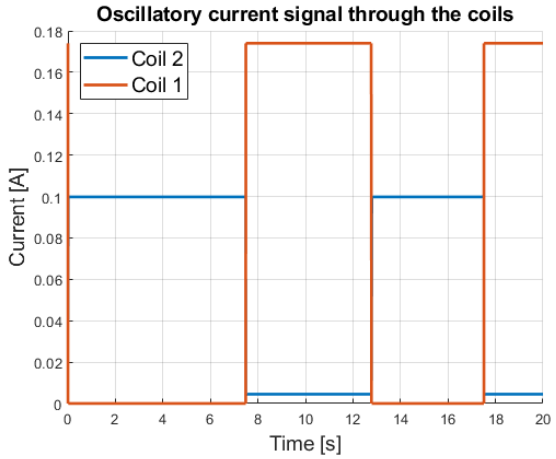

Figure 20: Simulation of the signal through the coils with parasitics. Coil 1 oscillates between 0 and 174.00 mA, has a frequency of 0.0997 Hz and a duty cycle of 52.77%. Coil 2 oscillates between 4.53 and 99.81 mA, has a frequency of 0.997 Hz and a duty cycle of 47.16%. The 'start-up' time is 7.49 seconds.

When the results from the circuit with parasitics (Figure 20) are compared to those without (Figure 16b), it is visible how the wires affect the signal. The frequency of both of the signals stays largely the same, with only a minimal difference in the duty cycle of coil 1 (52.79% compared to 52.77%). The current through coil 1 has changed from oscillating between 0 and 173.98 mA (Figure 16b) to oscillating between 0 and 174.00 mA (Figure 20). The current through coil 2 has changed from oscillating between 3.11 and 99.99 mA (Figure 16b) to oscillating between 4.53 and 99.81 mA (Figure 20).

IV. Discussion

While the electric circuit does fulfill its purpose, it is not of adequate quality yet to implement into a microrobot. There are still some aspects that need to be experimentally determined to provide deeper insight into the eventual design. This includes, but is not limited to: improvements to the current design, the buildup of the oscillatory signal, the use of two external magnetic fields, the required strength of the magnetic fields, the incorporation of an FC-stack into the circuit and the safety of a capsule with a FC in the human body.

First, the current design could be further improved upon. This can be done through the incorporation of more transistors, to give a higher current gain and to provide another function to the TFT, namely inversion. An example of an improved circuit is given in Figure 21 [17] with the corresponding signal in Figure 22.

Second, the oscillatory signal (as visible in Figure 18a) is currently in the form of a square wave, which means that it is either fully turned 'on' or fully turned 'off'. When one of the coils is fully turned 'on', this might cause the capsule to snap into place, instead of gradually reaching the correct orientation. If a gradual movement is desired, the buildup of the oscillatory signal should also be gradual, and not instant. If a gradual movement is not required, then the signal frequency should be adjusted to allow for a smooth rotation of the capsule, since the current frequency was chosen to be an arbitrary value.

Third, If the use of two external magnetic fields is not feasible, a singular external magnetic field will have to be used to improve upon the design. The oscillatory signal through the coils should then be changed accordingly since they would then have to generate both of

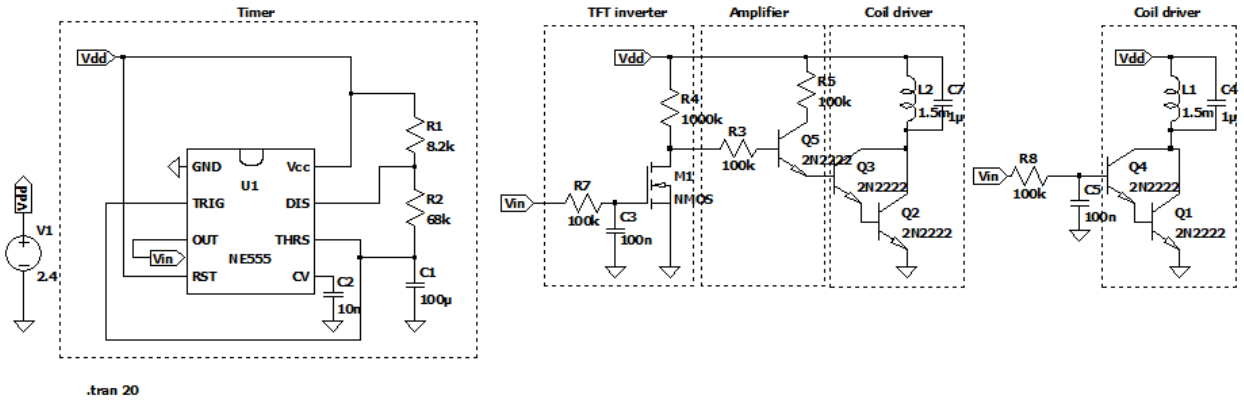

Figure 21: An improved circuit based on the current design with the TFTs acting as a signal inverter [17]. This circuit has a higher current flowing through the coils when compared to the current design, which can be adjusted based on the specific requirements.

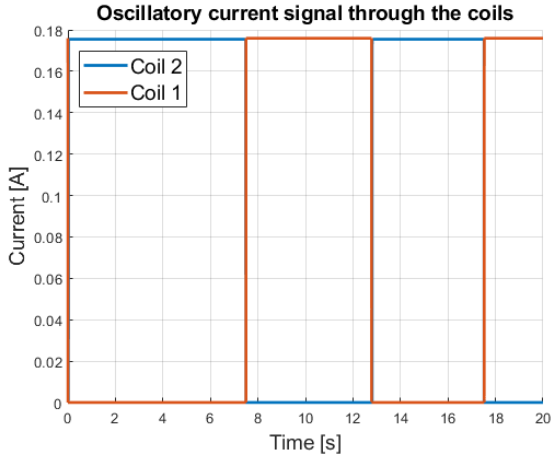

Figure 22: The signal based on the improved circuit design given in Figure 21.

the magnetic poles. This principle can be compared to the workings of a DC motor. One of the options to achieve this might be through the addition of H-bridges to the electric circuit, which can be constructed using either transistors or MOSFETs depending on the specific requirements. An example of this is given in Figure 23a [17]. One of the advantages of this circuit is that the energy that is stored within one coil, will transfer to the other during switching [17]. Another option might be through the use of a state machine, which represents the state of the coil(s) through binary values [17]. With the addition of so-called 'flip-flops', the circuit would be able to switch between these states [17].

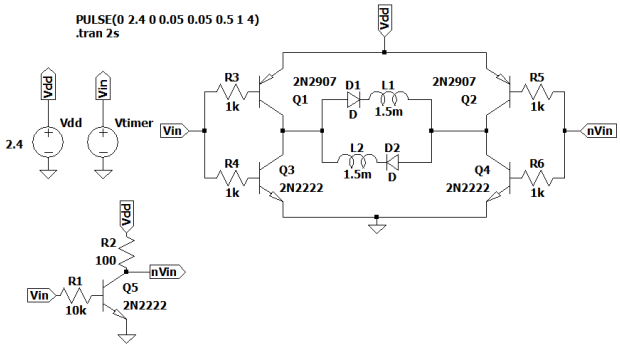

(a)

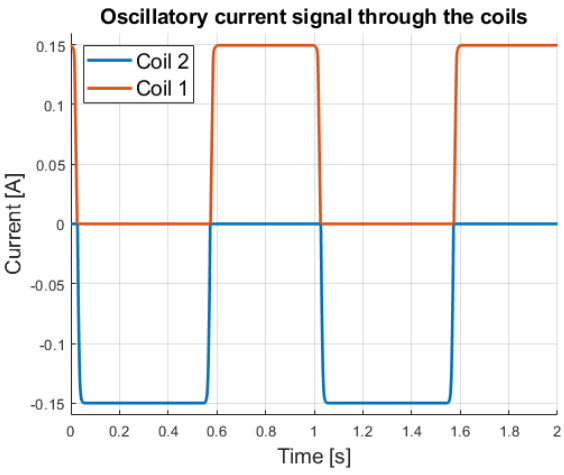

(b)

Figure 23: (a) Example of an H-bridge oscillatory circuit [17]. The circuit could be changed to fit the specific requirements. (b) Signal corresponding to the H-bridge oscillatory circuit.

Fourth, it is not completely clear whether the strength of the magnetic fields generated by the coils will be strong enough to allow for rotation. This, however, could

be compensated by increasing the strength of the external magnetic field(s).

Fifth, the FC-stack would have to be incorporated into the circuit to test if it works, instead of simulating the voltage output using a power source. The current circuit requires at most 2.4 V and 0.272 A (Figure 14). Judging from the IV characteristics of the FC (Figure 2), an FC-stack of 3 FCs might not barely be able to provide this voltage and amperage. This will result in less current flowing through the coils and thus decreasing the magnetic field strength generated by them.

Lastly, since the capsule should eventually be used in the human body, the safety of using a FC might be a cause for concern. FCs could be used for in vitro medical devices [10], but the design of the entire capsule should be completely safe for humans.

Apart from these aspects which would require further research, there are also aspects that will have to be added to allow the microrobot to be fully operable. The design currently includes two coils, which limits its capabilities to rotation. A third coil would have to be added to allow for three-dimensional movement. To manage the movement of the microrobot, a form of control will have to be added to the electric circuit. The eventual design also requires further downscaling, since the size is currently too large to be implemented into the human body.

A. *Future Research*

This design can be further improved and optimised, however, this does require more research on the topics of downscaling the design, lowering the power requirements and adding control to the design.

First, the design should be further downscaled in size to allow it to be used inside the human body. Currently, the capsule is estimated to require a diameter of 64 mm (II-A) to provide an adequate fit for the FC. The FC will have to be downscaled further which will decrease the voltage and amperage output. This leads to the second point of lowering the power requirements of the circuit. Since the power supply will be smaller, the circuit will have to be adjusted to fit the limited supply. The use of low-power electronics, such as the TFTs, can prove to be very useful in these circuits. In the case of limited power supply, voltage and/or current amplifiers (through the use of DC/DC step-up converters like the LTC3105 [27] and/or transistors respectively) could be added to the circuit to make up for the lack of power. Lastly, research will have to be done on adding control to the microrobot, to allow it to move freely in the human body. The control is also necessary to allow the microrobot to perform functions.

V. Conclusion

The goal of this thesis was to attempt to develop an electric circuit combining the concepts of microrobots, FCs and soft robotics to generate a magnetic moment. This was done through analysis of the properties of these components, designing the electric circuit, testing the circuit and comparing it to the simulated results. Analysing the properties of these components gave valuable insight into their characteristics. First, FCs are a great alternative for batteries and can be used inside the human body and TFTs can operate more effectively under low-power circumstances than their discrete counterparts. Second, The design of the electric circuit utilised these components and was able to meet the size requirements. Finally, the circuit was (after some minor changes) able to give an oscillatory current through both of the coils comparable to that of the simulation.

REFERENCES

1. Turrentine FE, Wang H, Simpson VB, and Jones RS. Surgical Risk Factors, Morbidity, and Mortality in Elderly Patients. Journal of the American College of Surgeons 2006; 203:865–77. DOI: https://doi.org/10.1016/j.jamcollsurg.2006.08.026. Available from: https://www.sciencedirect.com/science/article/pii/S107275150601369X
2. Nelson BJ, Kaliakatsos IK, and Abbott JJ. Microrobots for Minimally Invasive Medicine. Annual Review of Biomedical Engineering 2010; 12. PMID: 20415589:55–85. DOI: 10.1146/annurev-bioeng-010510-103409. eprint: https://doi.org/10.1146/annurev-bioeng-010510-103409. Available from: https://doi.org/10.1146/annurev-bioeng-010510-103409
3. Jang D, Jeong J, Song H, and Chung SK. Targeted drug delivery technology using untethered microrobots: a review. Journal of Micromechanics and Microengineering 2019; 29:053002. DOI: 10.1088/1361-6439/ab087d. Available from: https://dx.doi.org/10.1088/1361-6439/ab087d
4. Ullrich F, Bergeles C, Pokki J, Ergeneman O, Erni S, Chatzipirpiridis G, Pané S, Framme C, and Nelson BJ. Mobility Experiments With Microrobots for Minimally Invasive Intraocular Surgery. Investigative Ophthalmology & Visual Science 2013 Apr; 54:2853–63. DOI: 10.1167/iovs.13-11825. eprint: https://arvojournals.org/arvo/content_public/journal/iovs/933467/i1552-5783-54-4-2853.pdf. Available from: https://doi.org/10.1167/iovs.13-11825
5. Chowdhury S, Jing W, and Cappelleri DJ. Controlling multiple microrobots: recent progress and future challenges. Journal of Micro-Bio Robotics 2015; 10:1–11
6. Hwang J, Kim Jy, and Choi H. A review of magnetic actuation systems and magnetically actuated guidewire- and catheter-based microrobots for vascular interventions. Intelligent Service Robotics 2020; 13:1–14
7. Seyfried J, Szymanski M, Bender N, Estaña R, Thiel M, and Wörn H. The I-SWARM Project: Intelligent Small World Autonomous Robots for Micro-manipulation. *Swarm Robotics*. Berlin, Germany: Springer, 2005 :70–83. DOI: 10.1007/978-3-540-30552-1_7
8. Estaña R and Woern H. The MiCRoN Robot Project. *Autonome Mobile Systeme 2007*. Berlin, Germany: Springer, 2007 :334–40. DOI: 10.1007/978-3-540-74764-2_52
9. O'hayre R, Cha SW, Colella W, and Prinz FB. Fuel cell fundamentals. John Wiley & Sons, 2016
10. Xu Q, Zhang F, Xu L, Leung P, Yang C, and Li H. The applications and prospect of fuel cells in medical field: A review. Renewable Sustainable Energy Rev. 2017 Jan; 67:574–80. DOI: 10.1016/j.rser.2016.09.042
11. Cianchetti M, Laschi C, Menciassi A, and Dario P. Biomedical applications of soft robotics. Nat. Rev. Mater. 2018 Jun; 3:143–53. DOI: 10.1038/s41578-018-0022-y
12. Mekhilef S, Saidur R, and Safari A. Comparative study of different fuel cell technologies. Renewable Sustainable Energy Rev. 2012 Jan; 16:981–9. DOI: 10.1016/j.rser.2011.09.020
13. AFT Fluorotec. [Online; accessed 16. Jan. 2024]. 2024 Jan. Available from: https://www.fluorotec.com/news/blog/peek-and-hydrogen-embrittlement
14. [Online; accessed 12. Jan. 2024]. 2024 Jan. Available from: https://content.kemet.com/datasheets/KEM_L9008_SBCP.pdf
15. Pandey M, Rashiku M, and Bhattacharya S. Recent progress in the development of printed electronic devices. *Chemical Solution Synthesis for Materials Design and Thin Film Device Applications*. Walthm, MA, USA: Elsevier, 2021 Jan :349–68. DOI: 10.1016/B978-0-12-819718-9.00008-X
16. com html. alldatasheet. VN2222L Datasheet(3/4 Pages) VISHAY | N-Channel 60-V (D-S) MOSFETs with Zener Gate. [Online; accessed 12. Dec. 2023]. 2023 Dec. Available from: https://html.alldatasheet.com/html-pdf/116974/VISHAY/VN2222L/660/3/VN2222L.html
17. Abelmann L. "Private communication". 2024 Feb
18. Contributors to Wikimedia projects. 555 timer IC - Wikipedia. [Online; accessed 15. Jan. 2024]. 2023 Dec. Available from: https://en.wikipedia.org/w/index.php?title=555_timer_IC&oldid=1191754446
19. [Online; accessed 31. Jan. 2024]. 2023 Dec. Available from: https://www.ti.com/lit/ds/symlink/lmc555.pdf?ts=1706693406493&ref_url=https%253A%252F%252Fwww.mouser.es%252F
20. [Online; accessed 8. Feb. 2024]. 2022 Apr. Available from: https://www.mouser.com/datasheet/2/115/ZTX1048A-92228.pdf
21. [Online; accessed 7. Feb. 2024]. 2020 Dec. Available from: https://www.sra-shops.com/pub/media/docs/srasolder/datasheet/tds-kd-series.pdf
22. [Online; accessed 7. Feb. 2024]. 2019 Oct. Available from: https://docs.rs-online.com/2258/0900766b81568eb0.pdf
23. com alldatasheet. C547B PDF. [Online; accessed 7. Feb. 2024]. 2024 Feb. Available from: https://pdf1.alldatasheet.com/datasheet-pdf/view/16106/PHILIPS/C547B.html

24. com alldatasheet. BC549C PDF. [Online; accessed 7. Feb. 2024]. 2024 Feb. Available from: https://pdf1.alldatasheet.com/datasheet-pdf/view/2893/MOTOROLA/BC549C.html
25. [Online; accessed 1. Feb. 2024]. 2023 Jul. Available from: https : / / docs . rs - online . com / 6089 / A700000006677186.pdf
26. Küpper T. Evaluation of 50 Ω driver circuits for digital signals based on oscilloscope measurements. Heliyon 2021; 7
27. [Online; accessed 9. Feb. 2024]. 2020 Feb. Available from: https://www.analog.com/media/en/technical-documentation/data-sheets/3105fb.pdf

VI. Appendices

A. AI Disclosure

During the preparation of this work the author used Grammarly in order to conduct a final spelling/grammar check. After using this tool/service, the author reviewed and edited the content as needed and takes full responsibility for the content of the work.

B. Experimental Setup Images

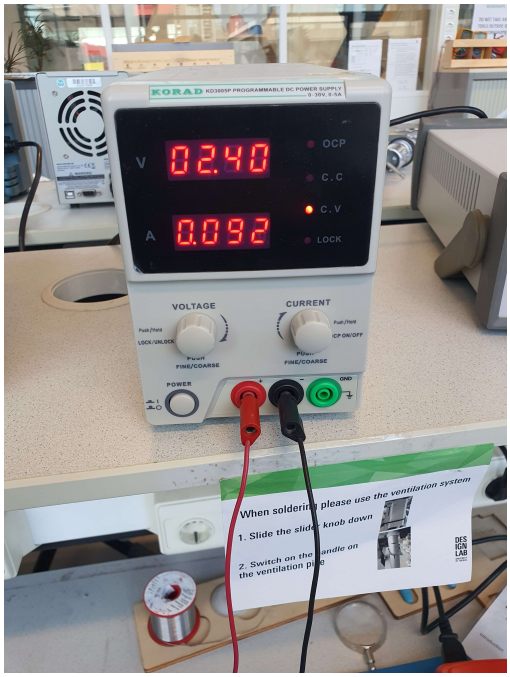

Figure 24: Minimum current requirement of the electric circuit.

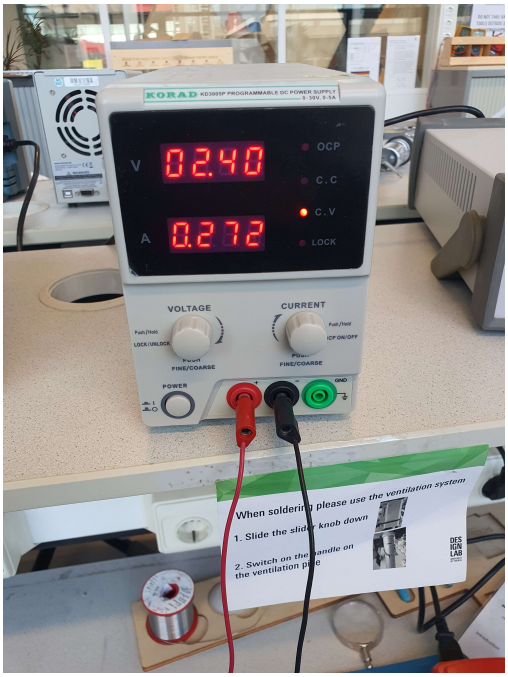

Figure 25: Maximum current requirement of the electric circuit.

Figure 26: The probes which measured the voltage over the coils did not amplify the signal (amplification of 1x).

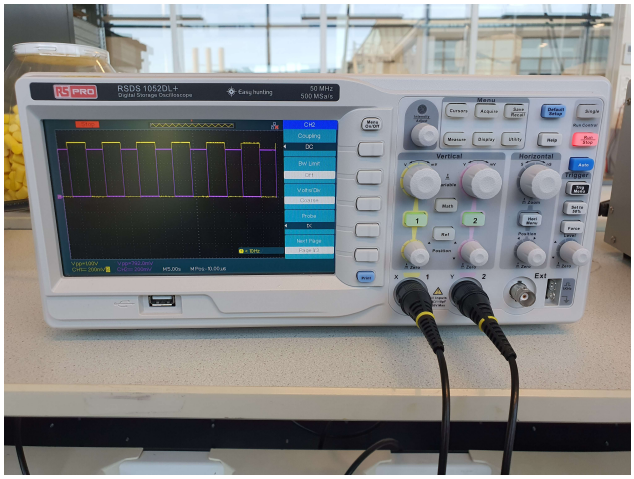

Figure 27: The oscilloscope did not amplify the signal received from the probes (amplification of 1x).